Research Article

Nathaniel Capote-Robayna, Ana I. F. Tresguerres-Mata, Aitana Tarazaga Martín-Luengo, Enrique Terán-García, Luis Martin-Moreno, Pablo Alonso-González* and Alexey Y. Nikitin*

Twist-tunable in-plane anisotropic polaritonic crystals

https://doi.org/10.1515/nanoph-2024-0462
Received September 4, 2024; accepted November 11, 2024; published online November 26, 2024

Abstract: van der Waals (vdW) materials supporting phonon polaritons (PhPs) – light coupled to lattice vibrations – have gathered significant interest because of their intrinsic anisotropy and low losses. In particular, α-MoO_3 supports PhPs with in-plane anisotropic propagation, which has been exploited to tune the optical response of twisted bilayers and trilayers. Additionally, various studies have explored the realization of polaritonic crystals (PCs) – lattices with periods comparable to the polariton wavelength. PCs consisting of hole arrays etched in α-MoO_3 slabs exhibit Bragg resonances dependent on the angle between the crystallographic axes and the lattice vectors. However, such PC concept, with a fixed orientation and size of its geometrical parameters, constrains practical applications and introduces additional scattering losses due to invasive fabrication processes. Here, we demonstrate a novel PC concept that overcomes these limitations, enabling low-loss optical tuning. It comprises a rotatable pristine α-MoO_3 layer located on a periodic hole array fabricated in a metallic layer. Our design prevents degradation of the α-MoO_3 optical properties caused by fabrication, preserving its intrinsic low-loss and in-plane anisotropic propagation of PhPs. The resulting PC exhibits rotation of the Bloch modes, which is experimentally visualized by scanning near-field microscopy. In addition, we experimentally determine the polaritons momentum and reconstruct their band structure. These results pave the way for mechanically tunable nano-optical components based on polaritons for potential lasing, sensing, or energy harvesting applications.

Keywords: hyperbolic polaritons; phonon polaritons; polaritonic crystals; twisted heterostructures; van der Waals materials; nanophotonics

1 Introduction

The discovery of polaritons supported by van der Waals (vdW) materials [1], [2] has sparked significant interest due to their potential for manipulating light on the nanoscale [3]. In particular, the propagation of in-plane anisotropic phonon polaritons (PhPs) is supported in certain crystal layers, such as calcite [4], α-MoO_3 [5], V_2O_5 [6], or bGO [7] among others. These materials exhibit PhPs with hyperbolic dispersion across specific frequency ranges, leading to exotic optical phenomena such as light canalization in twisted crystal bilayers [8]–[11] and trilayers [12], [13], or twist-tunable nanoresonators [14]. These findings open possibilities for an active tuning of the polariton propagation through the twist angle between layers, which is the key feature of the emerging field known as twistoptics. Another interesting option for controlling polaritons on the nanoscale consists of constructing polaritonic crystals (PCs) – lattices composed of elements periodically spaced at distances comparable to the wavelength of polaritons – made in vdW materials, such as, e.g., h-BN [15], α-MoO_3 [16]–[18], monolayer graphene [19], [20], or twisted bilayer graphene [21]. PCs support ultra-confined Bloch modes [22]–[24] that can favor a

***Corresponding authors: Pablo Alonso-González**, Department of Physics, University of Oviedo, Oviedo, 30006, Spain; and Center of Research on Nanomaterials and Nanotechnology, CINN (CSIC-Universidad de Oviedo), El Entrego, 33940, Spain, E-mail: pabloalonso@uniovi.es;
and **Alexey Y. Nikitin**, Donostia International Physics Center (DIPC), Donostia-San Sebastián, 20018, Spain; and IKERBASQUE, Basque Foundation for Science, Bilbao, 48013, Spain, E-mail: alexey@dipc.org.
https://orcid.org/0000-0002-2327-0164
Nathaniel Capote-Robayna, Applied Physics Department, Engineering School of Gipuzkoa, University of the Basque Country (UPV/EHU), Donostia-San Sebastián, 20018, Spain; and Donostia International Physics Center (DIPC), Donostia-San Sebastián, 20018, Spain.
https://orcid.org/0000-0002-8374-3218
Ana I. F. Tresguerres-Mata, **Aitana Tarazaga Martín-Luengo and Enrique Terán-García**, Department of Physics, University of Oviedo, Oviedo, 30006, Spain; and Center of Research on Nanomaterials and Nanotechnology, CINN (CSIC-Universidad de Oviedo), El Entrego, 33940, Spain. https://orcid.org/0000-0002-9530-9056 (A.I.F. Tresguerres-Mata). https://orcid.org/0000-0003-3049-1472 (E. Terán-García)
Luis Martin-Moreno, Instituto de Nanociencia y Materiales de Aragón (INMA), CSIC-Universidad de Zaragoza, Zaragoza, 50009, Spain; and Departamento de Física de la Materia Condensada, Universidad de Zaragoza, Zaragoza, 50009, Spain. https://orcid.org/0000-0001-9273-8165

topological funneling of PhPs [25]. Recently, PCs composed of hole arrays (HAs) in α-MoO_3 slabs have been suggested and studied, both theoretically [16] and experimentally [17], [18]. In these PCs, emerging Bragg resonances depend on the orientation of the lattice vectors with respect to the crystallographic axes of the vdW crystal layer. However, these HAs were etched directly in the anisotropic vdW layer, so that their geometry is not actively reconfigurable. Moreover, the fabrication of holes within the α-MoO_3 increases the optical losses due to severe scattering processes [22], [26]. Consequently, although the rotational dependence of the Bragg resonances has been showcased, achieving postfabrication tunability remains a challenge.

In this work, we introduce a novel PC concept based on the fabrication of twistable α-MoO_3/metal heterostructures that overcomes the above limitations, enabling low-loss optical tuning. As depicted in Figure 1, it comprises a twisted pristine layer of α-MoO_3 on top of a periodic HA made in a gold layer. Remarkably, the α-MoO_3 has been chosen due to its long polaritonic lifetimes, reaching up to 20 ps [5]. However, conceptually, it could be replaced by any other in-plane anisotropic material, such as V_2O_5 [6] or bGO [7], which provide similar twist-dependent properties. The lattice period matches the wavelengths of the PhPs in α-MoO_3 crystal on top of gold. This configuration allows for active tunability of the angle between the lattice vectors and crystallographic directions by rotating the α-MoO_3 layer. It is important to note that the parameters of our periodic HA are chosen to ensure the presence of "collective" lattice effects, in contrast to the periodic set of individual twist-tuneable Fabry–Perot resonators previously reported [14]. Employing a theoretical approach, which incorporates full-wave simulations and an analytical approximation, we describe the formation of PhP band structure and excitation of Bragg resonances. Furthermore, we conduct near-field measurements for different rotation angles, managing to disentangle the contribution of individual PhP Bloch modes emerging in this configuration. With our combined theoretical approach, we also reconstruct the PhP bands from the near-field data, by extracting the wavelength of the PhPs along different directions in plane.

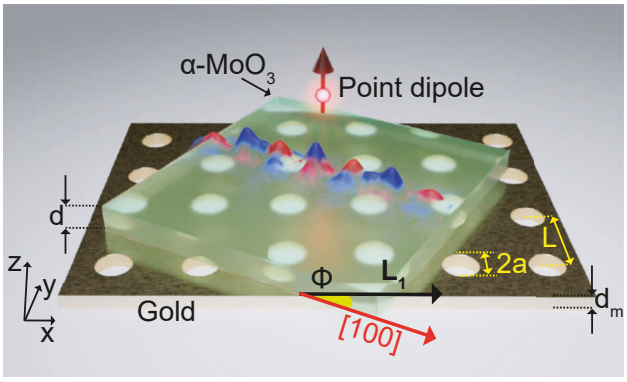

Figure 1: Schematic of a twist-tunable polaritonic crystal: an in-plane anisotropic α-MoO_3 layer twisted on top of a HA made on gold. The periodic lattice comprises a HA drilled in a gold layer with thickness d_m, hole radius a, and periodicity L. The anisotropic crystal layer, α-MoO_3, with thickness d, has its crystallographic axes twisted by an angle ϕ with respect to the lattice vectors. To visualize the polaritons excited in the PC, we modeled the distribution of the electric field (z-component), generated by a vertically oriented point dipole placed above the α-MoO_3 layer.

2 Results

In Figure 1, we show the schematics of our heterostructure representing a twisted PC. A pristine layer of α-MoO_3 (of thickness d) lies on a metallic film (of thickness d_m) with a periodic array of holes (of radius a and filled by a material with permittivity ϵ_h) etched in it. Although our concept is valid for any periodic lattice with arbitrary lattice vectors $\boldsymbol{L_1}$ and $\boldsymbol{L_2}$, here for simplicity we focus on a square lattice ($\boldsymbol{L_1}$ and $\boldsymbol{L_2}$ are orthogonal and $|\boldsymbol{L_1}| = |\boldsymbol{L_2}| = L$). The α-$MoO_3$ layer is twisted by an angle ϕ with respect to the $\boldsymbol{L_1}$ lattice vector of the HA. Notice that the thickness of the gold film is assumed to be larger than the skin depth, so that the PhPs in the vdW layer are not sensitive to d_m.

Crystal layers of α-MoO_3 support PhPs within three different Reststrahlen bands [27] (RBs, range of frequencies defined between the longitudinal and transversal optical phonons frequency, LO and TO, respectively): 544.6 cm^{-1} – 850.1 cm^{-1} for RB1, 821.4 cm^{-1} – 963 cm^{-1} for RB2, and 956.7 cm^{-1} – 1,006.9 cm^{-1} for RB3. In these RBs, the isofrequency curves (IFC) – describing available in-plane momenta at a fixed frequency – can take different shapes. Thus, in RB1 and RB2 IFCs have hyperbola-like shapes, with vertices lying on the [001] and [100] crystallographic directions, respectively. In contrast, PhPs with elliptical IFCs are supported in RB3. These highly anisotropic PhPs evolve into a series of modes, commonly designated as Mn, where $n \in \mathbb{N}$ indicates the quantization of the mode in the transversal (perpendicular to the slab) direction, displaying a lower propagation length and wavelength when increasing n. As in the mid-IR frequency range gold behaves as a perfect electric conductor (a "mirror"), only symmetrical modes could be excited in an α-MoO_3 layer on top of a gold film, so that the mode with the longest polaritonic wavelength is M1 [14].

To study and illustrate the emergence of tunable Bragg resonances in our twisted heterostructure, we first

consider illumination by a plane wave, i.e., the excitation of PhPs from the far-field. To that end, we calculate the field amplitudes of different diffraction orders (see Supplementary Material, Section 1 for details). The parameters of the lattice (period $L = 250$ nm, and the hole radius $a = 55$ nm, where the holes are filled by air, thus $\varepsilon_h = 1$) have been chosen to match the available wavelengths of the PhP mode in an α-MoO_3 slab of thickness $d = 70$ nm. This selection guarantees the presence of Bragg PhP resonances within the hyperbolic RB2. The hole radius is large enough to ensure strong collective Bragg resonances, yet small enough to prevent the formation of Fabry–Perot resonances that could interfere with collective Bragg modes. For simplicity, but without loss of generality, we assume that both the substrate and superstrate are air, while the thickness of the metal film is set to $d_m = 30$ nm. The light propagating through the PC is scattered into various diffraction orders (plane waves), which we labeled as (n_1, n_2). Their field amplitudes, $R_{\sigma n_1 n_2}$, (with $\sigma = s$, and $\sigma = p$ staying for s- and p-polarizations, respectively), can be individually determined from a linear system of equations (see Supplementary Material, Section 1, Eq. (77)). In Figure 2b, f, and j, we show the spectra of the normalized reflection coefficient, ΔR (solid black line), for three values of the twisting angle ϕ, as illustrated by the schematics in Figure 2a, e, and i. Here $\Delta R = R_b - R$, with R_b being the field amplitude of the (0, 0) order mode of an α-MoO_3 layer on top of an unstructured gold film, and R being the scattered amplitude of the (0, 0) order mode in the twisted PC. At $\phi = 0$ (Figure 2b), ΔR displays a peak at 885.1 cm^{-1}. At the same frequency, the $|R_{p10}|$ amplitude (blue curve) shows a clear resonant peak in its spectrum, indicating the emergence of a PhP Bragg resonance in (±1, 0) diffraction order. Indeed, the latter largely exceeds the contribution from the other nearest diffraction orders $|R_{p1-1}|$ and R_{p11}, as follows from their spectra, shown by the red and yellow lines, respectively. Apart from the

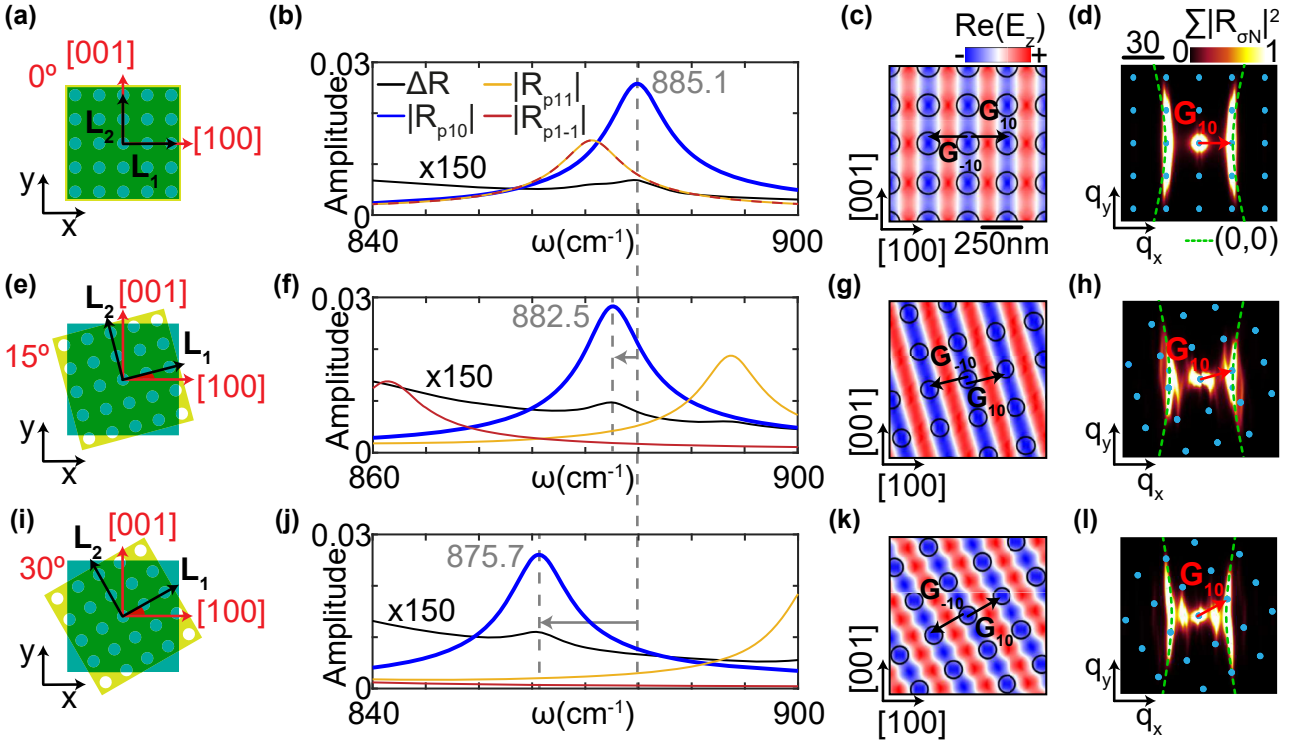

Figure 2: Twist-tunable Bragg resonances in a PC. (a, e, i) Schematics illustrating the top view of a twistable PC. The α-MoO_3 layer is aligned with the xy axis, whereas the gold HA (with the lattice vector basis, $\boldsymbol{L_1}$ and $\boldsymbol{L_2}$) undergo an anticlockwise twist of 0°, 15°, and 30°, respectively. (b, f, j) Spectra of different Fourier field harmonics amplitudes for normal incident light linearly polarized along the [100] axis. Black line represents $\Delta R = R_b - R$, where R_b is the reflection of α-MoO_3 on top of bare gold layer, and R is amplitude of the (0, 0) field harmonic. The blue, yellow, and red lines represent $|R_{p10}|$, $|R_{p11}|$, and $|R_{p1-1}|$ (p-polarization components of the Fourier field harmonics). The shift of the resonance is indicated by a gray dashed line. (c, g, k) Electric field distributions for $\phi = 0°$, 15°, and 30°, at the (±1, 0) resonance frequencies, 885.1 cm^{-1}, 882.5 cm^{-1}, and 875.7 cm^{-1}, respectively. The Bragg vector $\boldsymbol{G_{10}}$, perpendicular to the wave fronts and aligned to $\boldsymbol{L_1}$ lattice vector, is indicated by the black arrow. (d, h, l) Color plot (representing $\sum|R_{\sigma N}|^2$ for $\sigma \in \{s, p\}$) illustrates the IFC of the PC at the same twist angles and frequencies as in (c, g, k). The reciprocal lattice and the Bragg vector, $\boldsymbol{G_{10}}$, are indicated by the blue points and the red arrow, respectively. IFC of the empty lattice for the diffraction order (0, 0) is represented by the green dashed line.

(±1, 0) order mode, other Fourier field harmonics can also display resonant peaks, such as at 881.4 cm^{-1}, where the dominant amplitudes come from the (±1, ±1) and (±1, ∓1) orders. In these pairs, the sign of the left number matches the sign of the right number (up for up, down for down).

The emerging Bragg resonances can be explained by matching the IFC of the M1 PhP mode in the structure without holes with the reciprocal space vectors $\boldsymbol{G}_{\boldsymbol{n_1 n_2}} = n_1\boldsymbol{g_1} + n_2\boldsymbol{g_2}$, pointing from the origin toward the reciprocal space points (the grid of integers), marked by the blue dots in Figure 2d, h, and l. For instance, at 885.1 cm^{-1}, the IFC of the M1 PhP mode (indicated by the green dashed line in Figure 2d and also seen as the bright maxima of the color plot – see Supplementary Material, Section 2 for more details about color plot) meets the reciprocal vector $\boldsymbol{G_{10}}$, thus fulfilling the Bragg resonance condition for the (±1, 0) order. When the resonance condition is met, the electric field pattern, $E_z(x, y)$, represents a standing wave with the reciprocal vector $\boldsymbol{G_{10}}$, as shown in Figure 2c.

Next, we analyze the spectra of the PC when the α-MoO_3 layer is twisted by 15° and 30° with respect to the HA (schematics in Figure 2e and i), Figure 2f and j, respectively. In both cases, the frequency of the resonant peaks redshifts, to 882.5 cm^{-1} for $\phi = 15°$ and to 875.7 cm^{-1} for $\phi = 30°$, respectively, thus amounting up to ∼7 % of the entire RB. This twist-induced shift is also seen in the reciprocal space representations shown in Figure 2h and l. Due to the twist of the lattice in the real space, the reciprocal space points undergo an anticlockwise rotation. Because of the anisotropy of α-MoO_3, the dispersion relation depends upon the orientation of the k-vector and thus the dispersion curves. Consequently, the frequency at which the IFC meets the reciprocal vector $\boldsymbol{G_{10}}$ varies, so that the Bragg resonance condition is fulfilled at 882.5 cm^{-1} and 875.7 cm^{-1} for 15° and 30°, respectively. At these frequencies, the field patterns shown in Figure 2g and k clearly display a Bloch standing wave whose fringes are oriented along the $\boldsymbol{L}_1$ direction. Consistently, the major contribution into the excited PhP near-field arises from the diffraction order (±1, 0) with the dominating field amplitude, $\left|R_{p10}\right|$. Note that the Bragg resonance condition for other diffraction orders also shifts in frequency, as observed in the peak position of the field amplitudes $\left|R_{p11}\right|$ and $\left|R_{p1-1}\right|$. Actually, for nonzero Φ, their spectra no longer coincide, due to the break of symmetry. For instance, for $\Phi = 15°$, when the IFC meets $(1, 1)$ and $(-1, -1)$ reciprocal space points, it does not meet those at $(1, -1)$ and $(-1, 1)$. Finally, remark that the frequency tunability of the Bragg resonance by rotating the lattice with respect to the optical axes of the crystal layer remains an important intrinsic feature of twisted PCs [16], [17].

The dependence of the Bragg resonances upon the rotation angle is also encoded into the band structure of the twisted PC, which is illustrated in Figure 3. The volumetric Wigner–Seitz cell of the twisted PC is schematically shown in Figure 3a–c, together with the high symmetry points of the first Brillouin Zone (BZ). Apart from the square lattice symmetry points Γ, X, and M, we have introduced an additional point, X', as obviously due to the in-plane anisotropy of the α-MoO_3 layer, the PhP dispersion along [100] and the [010] axes is different. More specifically, the band structure along the path starting from Γ and finishing in X differs from that connecting Γ and X'. The color plot shown in Figure 3d illustrates the near-field intensity given by the summation of a large number of the field amplitudes, $R_{\sigma n_1 n_2}$, across the path $\Gamma -> X -> M -> \Gamma -> X' -> M$ (the arrows indicate the direction of the path, from the starting point to the end point) in the in-plane momentum plane. The bright maxima of the color plot approximately represent the "density of states" of PhP modes in the twisted PC. For a better interpretation of the band structure, we also plot in Figure 3d (gray dashed lines) the Φ-dependent empty grating dispersion branches, $\boldsymbol{k}_{\boldsymbol{n_1 n_2}}(\omega) = \boldsymbol{k}_{\boldsymbol{M1}}(\omega) + \boldsymbol{G}_{\boldsymbol{n_1 n_2}}$ (where $\boldsymbol{k}_{\boldsymbol{M1}}$ is the momentum of PhPs supported by α-MoO_3 on top of an unstructured metal film), for the diffraction orders $-2 \le n_1, n_2 \le 2$ and for $\Phi = 30°$. The empty grating dispersion finds an excellent agreement with the maxima of the color plot. Note that, the band gaps of the PhPs in the twisted PC are visually indistinguishable in the color plot. We attribute it to the low refractive index contrast, and thus the small reflectivity of the PhPs, by the areas of the holes. On the other hand, the dispersion branches of the twisted PC can be shifted by the twist angle, as illustrated in Figure 3e–h, showing a zoomed-in area within the blue dashed rectangle in Figure 3d. For instance in the Γ point, while at $\Phi = 0°$ the two branches $-\boldsymbol{k}_{\boldsymbol{M1}}(\omega) + \boldsymbol{G}_{10}$ and $\boldsymbol{k}_{\boldsymbol{M1}}(\omega) + \boldsymbol{G}_{-10}$ meet at 885.1 cm^{-1} (Figure 3e), by increasing Φ to 15°, 30°, and 45°, the crossing redshifts to 882.5 cm^{-1}, 875.7 cm^{-1}, and 863.9 cm^{-1}, respectively (in Figure 3f–h the shift is indicated by the gray dashed lines). To connect the tunability of the band structure with the Bragg resonance condition, in Figure 3i–l, we represent the IFCs at the crossing frequencies, 885.1 cm^{-1}, 882.5 cm^{-1}, 875.7 cm^{-1}, and 863.9 cm^{-1}, respectively. For the reference, the IFCs of the empty lattice PhPs with momenta $\pm\boldsymbol{k}_{\boldsymbol{M1}}$, $\pm\boldsymbol{k}_{\boldsymbol{M1}} + \boldsymbol{G}_{\pm 10}$, and $\pm\boldsymbol{k}_{\boldsymbol{M1}} + \boldsymbol{G}_{0\pm 1}$ are also rendered (green, yellow, and red dashed lines, respectively). For each Φ, we observe that the IFC meets the reciprocal space point (±1, 0) so that the Bragg resonance condition is fulfilled, implying the color plot maxima at this frequency at the Γ point observed in Figure 3e–h. Remark that, while our discussion has been

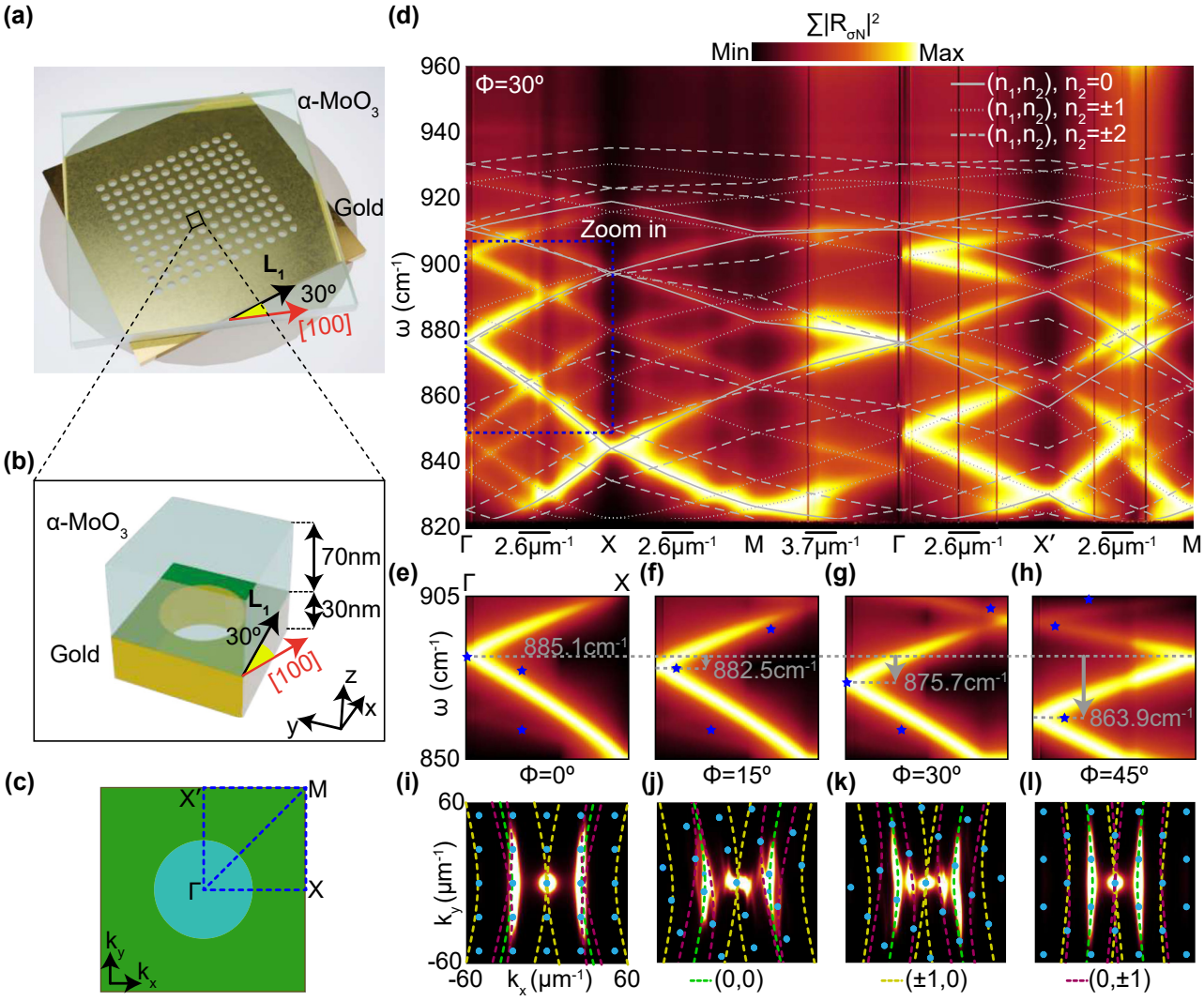

Figure 3: Tunability of the band structure of the twisted PC. (a) Schematic of the twisted PC for $\Phi = 30°$. (b) A zoom-in view of the Wigner–Seitz cell of the PC. The thickness of α-MoO_3 layer and the gold film at $d = 70$ nm, and $d_m = 30$ nm, respectively. (c) A sketch of the reciprocal space directions, indicated by blue dashed lines, with the main points of the BZ labeled as Γ, X, M, and X', respectively. The BZ is combined with a schematic of the x–y projection of the Wigner–Seitz cell. (d) Color plot (representing $\sum|R_{\sigma N}|^2$ for $\sigma \in \{s, p\}$) indicates the band structure of the twisted PC for $\Phi = 30°$. The empty lattice band structure is traced by the gray lines, for the diffraction orders $(n_1, 0)$, $(n_1, \pm 1)$, and $(n_1, \pm 2)$, with n_1 restricted to $-2 \leq n_1 \leq 2$. (e–h) Zoom-ins of the band structure for Φ of 0°, 15°, 30°, and 45°, respectively. The shift of the bands at the Γ point is indicated by the gray dashed lines and the arrow. The blue asterisk symbols indicate the extracted momentum from experiments (see details in Supplementary Material, Section 3). (i–l) Color plots indicating the IFCs of the twisted PC for Φ of 0°, 15°, 30°, and 45°, at the frequencies of 885.1 cm^{-1}, 882.5 cm^{-1}, 875.7 cm^{-1}, and 863.9 cm^{-1}, respectively. The reciprocal lattice is shown by the blue dots, and the IFCs of the empty lattice for the diffraction orders (0, 0), (±1, 0), and (0, ±1) are represented by the green, yellow, and red dashed lines, respectively.

centered on the zoomed-in region, these findings extend to the entire PhP band structure, so that all the bands undergo frequency shifts by twisting.

To corroborate our theoretical analysis, we conducted experimental near-field measurements on twisted PCs, which consist on a single α-MoO_3 layer placed on top of a gold film with a series of HA rotated at various angles (see Section 3). To visualize the PhPs Bloch modes, we employed near-field nanoimaging via scattering-type scanning near-field optical microscopy (s-SNOM) [23], see schematics in Figure 4a. The near-field excitation offers a significant advantage over the far-field approach, as (i) the latter is suppressed by the screening effect from the metal substrate and (ii) the s-SNOM tip allows one to access to large PhP momenta beyond the light cone. Both the sample and the s-SNOM tip are illuminated with a p-polarized mid-IR light at an incident frequency of 875.7 cm^{-1}, i.e., within the RB frequency range. By recording the scattered

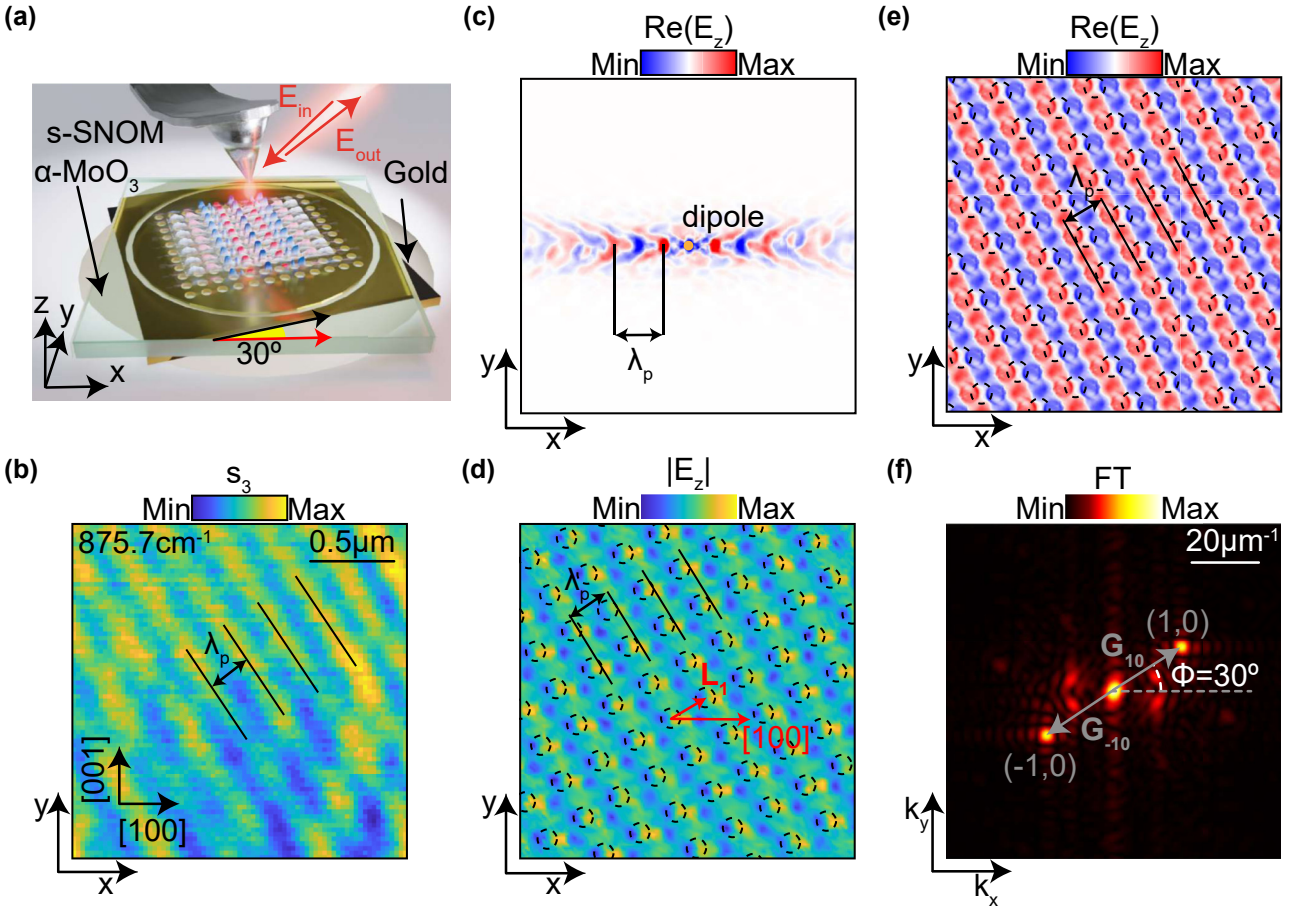

Figure 4: Near-field imaging of the PhP modes in the twisted PC and their analysis. (a) Schematics of the PC and the s-SNOM. The upper α-MoO_3 layer is twisted by $\Phi = 30°$ with respect to the HA in a thin gold layer. The structure is suspended in air, thus there is no substrate under the HA. An s-SNOM tip scans the PC under the presence of an incident field E_{in}, while the scattered field E_{out} is recorded. (b) A near-field s-SNOM image taken at the third harmonic at $\omega = 875.5\ \mathrm{cm}^{-1}$. Black lines indicate the fringes of the PhP Bloch wave. (c) The simulated $\mathrm{Re}\left[E_z(x,y)\right]$ generated by a vertical point dipole on top of a finite-size twisted PC. The wavelength of the PhP along the x-direction is indicated by the black lines. (d) Simulation of the near-field image shown in (b). The $\boldsymbol{L}_1$ vector of the reciprocal lattice and the [100] crystallographic axis from α-MoO_3 are indicated by the red arrows, whereas the position of the holes are marked by the black dashed circles. Black solid lines indicate the fringes. (e) Simulated $\mathrm{Re}\left[E_z(x,y)\right]$ generated by a normally incident plane wave polarized along [100] direction. Black lines indicate the fringes. (f) Color plot depicting the FTs of the near-field image shown in (b). The reciprocal space vectors $\boldsymbol{G}_{10}$ and $\boldsymbol{G}_{-10}$ are indicated by the gray arrows, forming an angle of 30° with respect to the k_x-axis.

field signal (s_3) (see Section 3), we produced the near-field images visualizing PhPs excited in the twisted PC at an angle $\Phi = 30°$ (color plot in Figure 4b). In the image, we observe a series of parallel fringes, marked by black solid lines, with a separation distance between them matching the periodicity of the HA. To interpret the observed near-field pattern, we conducted full-wave simulations employing a vertical point dipole source, mimicking the s-SNOM tip [23]. The simulated snapshot of $\mathrm{Re}(E_z)$ shown in Figure 4c reveals an oscillating field distribution (the wavelength is indicated by the black lines) within a narrow sector around the [100] crystallographic direction. This distribution is characteristic of recently reported canalized PhPs [9], [12]. The canalization regime of PhPs in our twisted PCs can be explained by the plane shape of the IFC of the M1 PhPs in an α-MoO_3 layer on top of a metal substrate, similar to α-MoO_3 on SiC [28]. Remarkably, such a directional pattern is produced by placing the dipole at any point above the twisted PC. Nevertheless, in the near-field image constructed by scanning the dipole in the x–y plane (Figure 4d, see Section 3, near-field full-wave simulations section), one can clearly recognize a standing wave pattern, in good agreement with the near-field measurements (Figure 4b). Such periodic pattern clearly indicates a largely collective nature of the excited electromagnetic fields, inherent to PCs. Moreover, in both simulated and experimental near-field images, the direction perpendicular to the fringes (highlighted by the solid black lines) forms a 30° angle with the [100] crystallographic axis,

thus being aligned with the lattice vector. This observation provides a hint that the $(\pm1, 0)$ Bloch mode is excited due to the $(\pm1, 0)$ Bragg resonance discussed above. To confirm our speculation, we performed full-wave simulations considering a normally incident plane wave illumination, thus completely excluding any effects induced by a localized source. The resulting distribution of $\mathrm{Re}(E_z)$ is illustrated in Figure 4e. The normally incident wave "acquires" the momentum $\boldsymbol{G}_{\pm10}$ provided by the lattice, so that the two excited contrapropagating PhPs plane waves form the $(\pm1, 0)$ Bloch mode, which can be recognized in Figure 4e. Its field distribution agrees well in shape, wavelength, and fringe orientation with the near-field images in Figure 4b and d. Furthermore, by representing the Fourier transform (FT) of the experimental near-field image as a color plot in Figure 4f, we can observe two bright maxima labeled as $(1, 0)$ and $(-1, 0)$ that perfectly match the lattice vectors, $\boldsymbol{G}_{\pm10}$. Overall, our simulations are consistent with our assumption that PhP Bloch mode is observed in the nanoimaging experiments.

Our PhP nanoimaging experiments can be extrapolated to other twist angles, Φ, as illustrated in Figure 5a–d. From panels a–d, α-MoO_3 layer maintains its crystallographic axes [100] and [001] aligned with the x and y axes, respectively, whereas the HA is twisted anticlockwise. In Figure 5a–d, the near-field images are shown at frequencies 884.3 cm^{-1}, 882.2 cm^{-1}, 875.7 cm^{-1}, and 864.1 cm^{-1}, corresponding to $(\pm1, 0)$ Bragg resonance condition for $\Phi = 0°$, 15°, 30°, and 45°, respectively (near-field images of PhP Bloch modes in other diffraction orders (n_1, n_2) apart from $(\pm1, 0)$ are shown in Supplementary Material, Section 4). Note that the case of $\Phi = 30°$ in Figure 5e and f is intentionally copied from Figure 4b, d, and f for a better visualization of Bragg resonance rotation as the twisting angle increase. For each twisting angle, a standing wave with fringes perpendicular to the $\boldsymbol{L}_1$ lattice vector is observed, where the fringe positions are indicated by black solid lines. These measurements are in good agreement with the full-wave simulations conducted via the scanning dipole method, shown in Figure 5e–h. To analyze the PhP wavelength and the orientation of the fringes, we performed FTs of the near-field data, represented as color plots in the insets of Figure 5a–d. The positions of the FT maxima confirm that the reciprocal lattice vector, $\boldsymbol{G}_{10}$, is twisted by an angle Φ with respect to the x axis. Specifically, for $\Phi = 45°$ in the near-field image (Figure 5d and h), in addition to the standing wave with fringes oriented along the lattice vector $\boldsymbol{L}_1$, we observe another standing wave oriented along

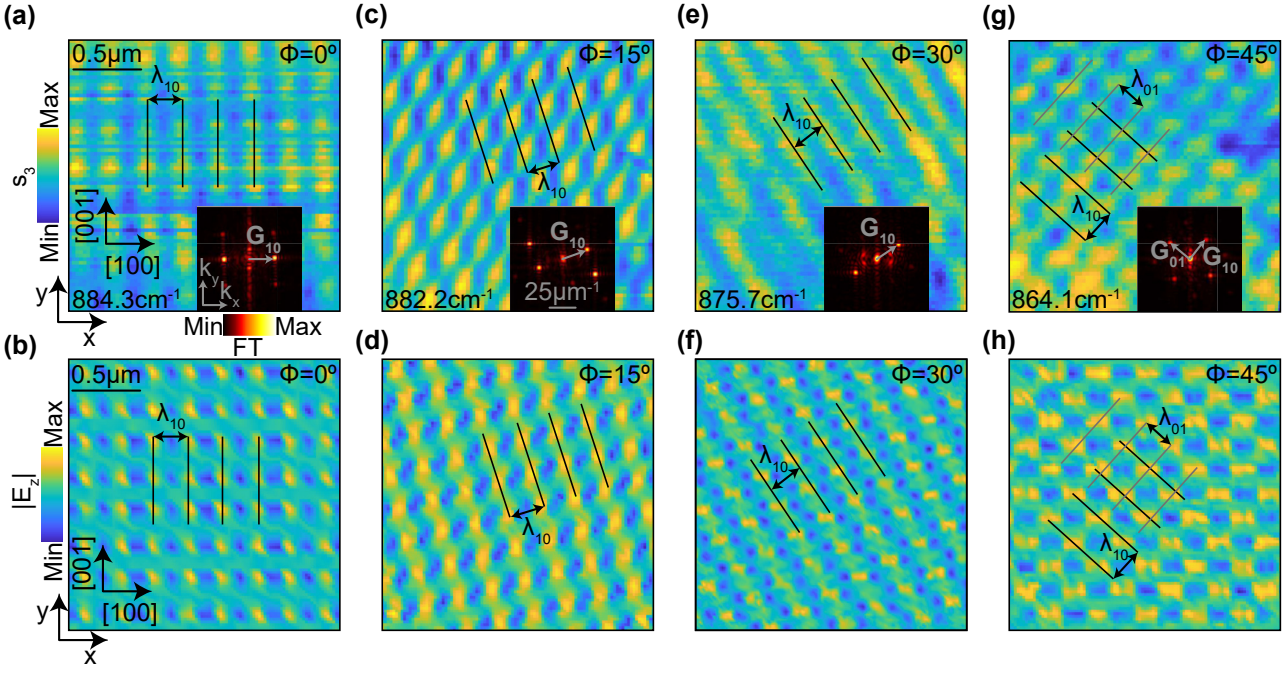

Figure 5: Near-field imaging of the twist-tunable PC for different twist angles. (a, c, e, g) s-SNOM near-field images for twist angles of $\Phi = 0°$, 15°, 30°, and 45° at the frequency of 884.3 cm^{-1}, 882.2 cm^{-1}, 875.7 cm^{-1}, and 864.1 cm^{-1}, respectively. Color plots representing the FTs of the near-field images for each Φ are included as insets, where the reciprocal lattice vectors, $\boldsymbol{G}_{10}$ and $\boldsymbol{G}_{01}$, are indicated by the gray arrows. (b, d, f, h) Simulated near-field images for a finite-size twisted PC, for the Φ and ω as in (a, c, e, g). The black solid lines indicate the fringes of the Bloch PhP wave in $(\pm1, 0)$ diffraction orders, while in (g, h) the gray lines indicate those in $(0, \pm1)$ diffraction orders.

$\boldsymbol{L}_2$ lattice vector (the fringes are indicated by gray lines). The appearance of the second standing wave arises due to the lattice symmetry. Indeed, for smaller twist angles, the Bragg resonance condition was fulfilled for two reciprocal lattice vectors, $\boldsymbol{G}_{\pm 10}$, since the IFC of the α-MoO_3 simultaneously intersects with only two reciprocal space points, namely $(\pm 1, 0)$. However, for $\Phi = 45°$, the crystallographic axes of α-MoO_3 are positioned such that the intersection of the IFC with four reciprocal space points, $(\pm 1, 0)$ and $(0, \pm 1)$, becomes possible. This effect becomes even clearer in the Fourier transform of the measured data shown in the inset of Figure 5d, where four bright maxima match with reciprocal lattice vectors $\boldsymbol{G}_{10}$ and $\boldsymbol{G}_{01}$. Using our near-field images, it is also possible to reconstruct the momentum of the PhP Bloch modes for each angle Φ by measuring the separation distance between the fringes, λ_{exp} (details provided in Supplementary Material, Section 3). Due to the limited efficiency of exciting Bragg mode solely via the lattice, a circular ring surrounding the PC was introduced to boost the near-field, thereby enhancing the generation of polaritonic Bragg modes in the HA region. The s-SNOM tip detects the scattered near-field and evanescent waves generated by the interaction between the ring and the HA, allowing us to map the resulting polaritonic modes. We then translate the measured wavelength into momentum space ($G_{\mathrm{exp}} = 2\pi/\lambda_{\mathrm{exp}}$), which falls into the second BZ. To properly represent this momentum in the band structure, we fold this momentum from the second BZ to the first BZ by subtracting $g_1 - G_{\mathrm{exp}}$. This folded momentum is depicted by blue asterisk symbols in Figure 3e–h, in good agreement with the theoretical predictions. Overall, in Figure 5, we have experimentally demonstrated tunability of Bloch modes by the twist angle.

To summarize, we have introduced and experimentally realized a tunable PC based on a heterostructure consisting of a twistable α-MoO_3 crystal layer on top of a gold HA. In stark contrast to previously reported twisted PCs, our design preserves the pristine α-MoO_3 layer and allows it to be rotated without the need to modify the lattice beneath it. While by the theoretical analysis we have demonstrated the twist-tuneability of the emerging Bragg resonances in our PC, our experiments clearly demonstrate the tuneability of the PC band structure and the polaritonic Bloch modes. Remarkably, collective lattice effects largely dominate the natural polaritonic canalization effect. The latter is due to the intrinsically flat isofrequency curve of polaritons in a crystal layer above a metal substrate. Importantly, although demonstrated for α-MoO_3, our general concept is valid for any similar heterostructure based on in-plane anisotropic crystal layers supporting polaritons. It is important to note that, while twist-tunable systems have already shown great promise for real-time optoelectronic applications, several challenges remain before they can be fully implemented. Advances in microelectromechanical systems [29] are expected to provide precise and rapid control of twist angles at the nanoscale, enabling high-speed, real-time tuning. Additionally, mechanical robustness, particularly under repeated twisting cycles, is also critical, as these systems must maintain their structural integrity and performance over time. Despite these challenges, ongoing efforts to integrate twist-tunable systems into scalable platforms compatible with existing optoelectronic technologies are yielding promising results. Our findings expand the vision of twistoptics in a wide perspective and particularly hold promise for the development of actively rotatable two-dimensional polaritonic elements.

3 Methods

3.1 Fabrication of the samples

The gold HA samples were provided by the company NanoStruct GmbH. The sample consists of a gold film with a circular hole of 100 μm in diameter, placed on top of pristine glass. Simultaneously, a gold single crystal is fabricated via wet chemical synthesis [30], and subsequently transferred on top of the hole in the gold/glass substrate, ensuring a small physical overlap between the gold single crystal and the gold film. This setup allows the gold single crystal to present a gold/glass interface while being easily connected electrically to the sample holder via the gold film. The HAs are structured with focused ion beam milling (with a Ga source from a Zeiss Orion NanoFab), employing a 30 kV and 30 pA current, and a dwell time of 1 μs with 20 repeats. Furthermore, layers of α-MoO_3 with a thickness of about 70 nm were exfoliated on top of the gold HAs through the application of a dry-transfer process [31]. The process began with a mechanical exfoliation of α-MoO_3 from commercially available bulk crystals sourced from Alfa Aesar, using Nitto tape (Nitto Denko, SPV 224P). Then, the α-MoO_3 flakes were transferred from the tape to a transparent stamp made of poly-(dimethylsiloxane) (PDMS). Only the uniform flakes were selected using an optical microscope examination. Finally, a micromanipulator was used to precisely position the PDMS stamp with the α-MoO_3 flake onto the targeted area on the substrate before smoothly detaching the flake (dry-transfer technique).

3.2 Near-field measurements

The near-field optical studies were conducted using a state-of-the-art scattering-type scanning near-field optical microscope (s-SNOM, Neaspec GmbH), equipped with quantum cascade lasers from Daylight Solutions, which covered a spectral range of 850–1,140 cm^{-1}. The s-SNOM combines an atomic force microscope (AFM) that operates in tapping mode with a frequency of approximately 285 kHz, a tapping amplitude near 200 nm, and commercially available metal-coated (Pt/Ir) AFM tips (ARROW-NCPt-50, Nanoworld). The process involved directing p-polarized mid-infrared light at the sample surface and focusing the light scattered back by the tip onto an infrared detector (Komar Technologies) using a parabolic mirror. We employed a pseudoheterodyne interferometric approach to decode the amplitude and phase of the signal, and the signal was demodulated at the third harmonic (the signal amplitude is denoted as s_3) to minimize the influence of far-field background scattering.

3.3 Mode expansion calculations

We develop an analytical theory based on Maxwell's equations. We represented electromagnetic fields as quasi-eigenmodes in our four-region structure. The four regions are (1) an isotropic superstrate characterized by permittivity ε_1 (we considered air, $\varepsilon_1 = 1$); (2) a biaxial layer (α-MoO_3) with a 3×3 permittivity tensor $\hat{\varepsilon}$ and thickness d; (3) the gold HA (metal film with the thickness d_m, lattice vectors $\boldsymbol{L}_1$ and $\boldsymbol{L}_2$, and hole radius a, where the holes are filled by air, thus $\varepsilon_h = 1$); and (4) the isotropic substrate, with the dielectric permittivity ε_4. The theoretical framework is based on two key assumptions: (i) the use of the quasi-orthogonal basis vectors to describe wave propagation within an infinite continuous anisotropic slab [32] and (ii) the approximation of the metal film by a perfect electric conductor – which is common and reasonable in the considered frequency range – so that the electromagnetic fields can only exist inside the holes [33]. More details are provided in the Supplementary Material, Section 1. The resulting dispersion relation implies an infinite sum over all the spatial field harmonics. This set of harmonics was truncated to $\max(|n_1|) = \max(|n_2|) = 12$.

3.4 Far-field full-wave simulations

Full-wave simulations of infinite PC illuminated by a normal plane wave, based on the finite-element method in the frequency domain, were performed using COMSOL. We considered an infinite two-dimensional square periodic gold HA with the thickness $d_m = 30$ nm, period $L = 250$ nm, and the hole radius $a = 55$ nm, where the holes are filled by air ($\varepsilon_h = 1$). On top, we place a α-MoO_3 layer with thickness $d = 70$ nm, whose crystallographic axes are twisted $-30°$ respect to the x–y plane. Both the superstrate and substrate are set as air, thus $\varepsilon_1 = \varepsilon_4 = 1$. A normal incident plane wave linearly polarized along the [100] crystallographic axis.

3.5 Near-field full-wave simulations

For the scanning point dipole simulations, we employed full-wave simulations using COMSOL. We modeled a finite 10×10 two-dimensional square periodic gold HA with thickness $d_m = 30$ nm, period $L = 250$ nm, and the hole radius $a = 55$ nm, where the holes are filled by air ($\varepsilon_h = 1$). The lattice vector $\boldsymbol{L}_1$ is twisted at a certain positive angle Φ with respect to [100] crystallographic axis, and the entire HA is surrounded by an air crown gap with inner diameter of 3.5 μm and outer diameter of 4 μm, mimicking the experimental setup, illustrated in Figure 4a. On top, we place a α-MoO_3 layer with thickness $d = 70$ nm, with crystallographic axis [100] located in the x axis. Both the superstrate and substrate are set as air, thus $\varepsilon_1 = \varepsilon_4 = 1$. A vertically oriented point dipole is placed at 300 nm distance from the surface, while $|E_z|$ field component is recorded at 20 nm from the surface, at the same x–y position as the dipole. The dipole is scanned in the x–y plane.

Research funding: The authors acknowledge Spanish Ministry of Science and Innovation (grants PID2020-115221 GB-C41, PID2020-115221 GB-C42, PID2023-147676NB-I00, PID2022-141304NB-I00, and PID2019-111156 GB-I00). AYN acknowledges the Basque Department of Education (grant PIBA-2023-1-0007). PA-G acknowledges support from the European Research Council under starting grant no. 101044461, TWISTOPTICS. LM-M acknowledges the Aragon Government through Project Q-MAD. AIFT-M and ET-G acknowledge the support from the Severo Ochoa program of the Government of the Principality of Asturias (nos. PA-21-PF-BP20-117 and PA-23-PF-BP22-046, respectively).

Author contributions: PA-G and AYN conceived the study and supervised the project. AIFT-M, ATM-L, and ET-G fabricated the samples and carried out the near-field imaging experiments. NC-R carried out the numerical simulations and mode expansion calculations, supervised by LM-M. NC-R, AIFT-M, ATM-L, and ET-G participated in the data analysis. NC-R and AYN cowrote the manuscript with input from the rest of the authors.

Conflict of interest: Authors state no conflicts of interest.

Informed consent: Informed consent was obtained from all individuals included in this study.

Ethical approval: The conducted research is not related to either human or animals use.

Data availability: The datasets generated and/or analyzed during the current study are available from the corresponding author upon reasonable request.

References

[1] D. N. Basov, M. M. Fogler, and F. J. G. de Abajo, "Polaritons in van der Waals materials," *Science*, vol. 354, no. 6309, p. aag1992, 2016.

[2] T. Low, *et al*., "Polaritons in layered two-dimensional materials," *Nat. Mater.*, vol. 16, no. 2, pp. 182—194, 2017.

[3] Q. Zhang, *et al*., "Interface nano-optics with van der Waals polaritons," *Nature*, vol. 597, no. 7875, pp. 187—195, 2021.

[4] W. Ma, *et al*., "Ghost hyperbolic surface polaritons in bulk anisotropic crystals," *Nature*, vol. 596, no. 7872, pp. 362—366, 2021.

[5] W. Ma, *et al*., "In-plane anisotropic and ultra-low-loss polaritons in a natural van der Waals crystal," *Nature*, vol. 562, no. 7728, pp. 557—562, 2018.

[6] J. Taboada-Gutiérrez, *et al*., "Broad spectral tuning of ultra-low-loss polaritons in a van der Waals crystal by intercalation," *Nat. Mater.*, vol. 19, no. 9, pp. 964—968, 2020.

[7] N. C. Passler, *et al*., "Hyperbolic shear polaritons in low-symmetry crystals," *Nature*, vol. 602, no. 7898, pp. 595—600, 2022.

[8] G. Hu, *et al*., "Topological polaritons and photonic magic angles in twisted α-MoO_3 bilayers," *Nature*, vol. 582, no. 7811, pp. 209—213, 2020.

[9] J. Duan, *et al*., "Twisted nano-optics: manipulating light at the nanoscale with twisted phonon polaritonic slabs," *Nano Lett.*, vol. 20, no. 7, pp. 5323—5329, 2020.

[10] M. Chen, *et al*., "Configurable phonon polaritons in twisted α-MoO_3," *Nat. Mater.*, vol. 19, no. 12, pp. 1307—1311, 2020.

[11] Z. Zheng, *et al*., "Phonon polaritons in twisted double-layers of hyperbolic van der Waals crystals," *Nano Lett.*, vol. 20, no. 7, pp. 5301—5308, 2020.

[12] J. Duan, *et al*., "Multiple and spectrally robust photonic magic angles in reconfigurable α-MoO_3 trilayers," *Nat. Mater.*, vol. 22, no. 7, pp. 867—872, 2023.

[13] C. Zheng, G. Hu, X. Liu, X. Kong, L. Wang, and C.-W. Qiu, "Molding broadband dispersion in twisted trilayer hyperbolic polaritonic surfaces," *ACS Nano*, vol. 16, no. 8, pp. 13241—13250, 2022.

[14] O. G. Matveeva, *et al*., "Twist-tunable polaritonic nanoresonators in a van der Waals crystal," *Npj 2D Mater. Appl.*, vol. 7, no. 1, p. 31, 2023.

[15] S. Dai, *et al*., "Tunable phonon polaritons in atomically thin van der Waals crystals of boron nitride," *Science*, vol. 343, no. 6175, pp. 1125—1129, 2014.

[16] N. Capote-Robayna, O. G. Matveeva, V. S. Volkov, P. Alonso-González, and A. Y. Nikitin, "Twisted polaritonic crystals in thin van der Waals slabs," *Laser Photon. Rev.*, vol. 16, no. 9, p. 2200428, 2022.

[17] J. Lv, *et al*., "Hyperbolic polaritonic crystals with configurable low-symmetry Bloch modes," *Nat. Commun.*, vol. 14, no. 1, p. 3894, 2023.

[18] N. R. Sahoo, *et al*, "Polaritons in photonic hypercrystals of van der Waals materials," *Adv. Funct. Mater.*, vol. 34, no. 41, p. 2316863, 2024.

[19] A. Y. Nikitin, F. Guinea, and L. Martin-Moreno, "Resonant plasmonic effects in periodic graphene antidot arrays," *Appl. Phys. Lett.*, vol. 101, no. 15, p. 151119, 2012.

[20] L. Xiong, *et al*., "Photonic crystal for graphene plasmons," *Nat. Commun.*, vol. 10, no. 1, p. 4780, 2019.

[21] S. S. Sunku, *et al*., "Photonic crystals for nano-light in moiré graphene superlattices," *Science*, vol. 362, no. 6419, pp. 1153—1156, 2018.

[22] F. J. Alfaro-Mozaz, *et al*., "Deeply subwavelength phonon-polaritonic crystal made of a van der Waals material," *Nat. Commun.*, vol. 10, no. 1, p. 42, 2019.

[23] F. J. Alfaro-Mozaz, *et al*., "Hyperspectral nanoimaging of van der Waals polaritonic crystals," *Nano Lett.*, vol. 21, no. 17, pp. 7109—7115, 2021.

[24] J. Yang, *et al*., "Near-field excited archimedean-like tiling patterns in phonon-polaritonic crystals," *ACS Nano*, vol. 15, no. 5, pp. 9134—9142, 2021.

[25] S. Guddala, *et al*., "Topological phonon-polariton funneling in midinfrared metasurfaces," *Science*, vol. 374, no. 6564, pp. 225—227, 2021.

[26] P. Li, *et al*., "Infrared hyperbolic metasurface based on nanostructured van der Waals materials," *Science*, vol. 359, no. 6378, pp. 892—896, 2018.

[27] G. Álvarez-Pérez, *et al*., "Infrared permittivity of the biaxial van der Waals semiconductor α-MoO_3 from near- and far-field correlative studies," *Adv. Mater.*, vol. 32, no. 29, p. 1908176, 2020.

[28] J. Duan, *et al*., "Canalization-based super-resolution imaging using a single van der Waals layer," *arXiv:2404.14876*, 2024.

[29] H. Tang, *et al*., "On-chip multi-degree-of-freedom control of two-dimensional materials," *Nature*, vol. 632, no. 8027, pp. 1038—1044, 2024.

[30] E. Krauss, *et al*., "Controlled growth of high-aspect-ratio single-crystalline gold platelets," *Cryst. Growth Des.*, vol. 18, no. 3, pp. 1297—1302, 2018.

[31] A. Castellanos-Gomez, *et al*., "Deterministic transfer of two-dimensional materials by all-dry viscoelastic stamping," *2D Mater.*, vol. 1, no. 1, p. 011002, 2014.

[32] G. Álvarez-Pérez, K. V. Voronin, V. S. Volkov, P. Alonso-González, and A. Y. Nikitin, "Analytical approximations for the dispersion of electromagnetic modes in slabs of biaxial crystals," *Phys. Rev. B*, vol. 100, no. 23, p. 235408, 2019.

[33] A. Roberts, "Electromagnetic theory of diffraction by a circular aperture in a thick, perfectly conducting screen," *J. Opt. Soc. Am. A*, vol. 4, no. 10, pp. 1970—1983, 1987.

Supplementary Material: This article contains supplementary material (https://doi.org/10.1515/nanoph-2024-0462).